Quasiparticle interference of spin momentum locked surface states at step edges on Re(0001)

J. Regel,* T. Mashoff, and H. J. Elmers
Institut für Physik, Johannes Gutenberg-Universität, Staudingerweg 7, D-55099 Mainz, Germany

(Received 25 June 2020; revised 12 August 2020; accepted 14 August 2020; published 8 September 2020)

Quasiparticle interference patterns formed by a surface state on the Re(0001) surface were investigated using scanning tunneling spectroscopy. The energy dispersion is inferred from Fourier-transformed differential conductivity maps for occupied and unoccupied states. The band dispersion for occupied states agrees with earlier published results obtained by angle-resolved photoemission spectroscopy. An analysis of the phase of interference patterns at step edges reveals a drastic change in the effective energy barrier for backscattering above and below the Fermi level. The attenuation of the interference pattern with increasing distance indicates interband scattering is the dominant scattering mechanism. Step decoration by Ni has a negligible influence on the pattern, excluding spin-flip scattering as a dominant contribution. The one-dimensional Re/Au line interface, however, reverses the scattering barrier behavior, indicating a coupling of surface states.

DOI: 10.1103/PhysRevB.102.115404

I. INTRODUCTION

It is known that the broken inversion symmetry at surfaces can lead to a lifting of the spin degeneracy of surface states. Such degeneracy lifting is most pronounced at the surface of high-Z materials [1]. The spin momentum locking of the surface states results in orthogonal wave functions provisionally eliminating backscattering. A similarly forbidden backscattering of surface states is responsible for the particular properties of topological insulators. Therefore, the study of scattering processes of spin momentum locked surface states is of growing interest [2,3].

The central question is how effectively spin momentum locking suppresses quantum interference and how one can tailor the scattering amplitude by material design. Controversial explanations for the occurrence of quantum interference have been discussed: For Rashba-split surface states, spin-conserving interband scattering can contribute to interference [4–6]. Alternatively, quantum interference patterns may result from nonorthogonal states causing only a partial suppression of backscattering [7–9]. Breaking the time-reversal symmetry with a magnetic material could also activate forbidden scattering channels [10–12].

The Re(0001) surface is an interesting system potentially suitable for solving this controversy [13,14]. A surface state is localized at the topmost atomic layer [15,16], and the orbital d_z^2 character is favorable for detection by scanning tunneling spectroscopy (STS). The strong spin-orbit coupling of Re leads to a pronounced Rashba splitting [17,18].

Here, we present an experimental study of quantum interference patterns on Re(0001) dependent on the electron energy using STS. We analyze the influence of submonolayer coverages of Au and Ni on the backscattering properties of the surface state. In order to identify the mechanism of backscattering we analyze the attenuation and phase of the quantum interference pattern at step edges.

II. EXPERIMENTAL METHODS

All experiments were conducted on a low-temperature scanning tunneling microscope (STM) at $T = 4.6\,\mathrm{K}$ in ultrahigh vacuum with commercial etched tungsten tips. The Re(0001) single crystal is prepared by alternate flashing at $T \approx 1800\,\mathrm{K}$ for around $t = 10\,\mathrm{s}$ and annealing in an oxygen atmosphere of $3 \times 10^{-8}\,\mathrm{mbar}$ at $T \approx 1400\,\mathrm{K}$ for 10 min, resulting in a nearly clean surface [19]. The step decorations are grown by deposing one tenth of a monolayer of Ni or Au via molecular beam epitaxy onto the cleaned Re(0001) surface and annealing at $T \approx 750\,\mathrm{K}$ for $t = 300\,\mathrm{s}$. Thus, narrow stripes of the adsorbed metals form at the step edges of Re. The sample is then transferred *in situ* into the STM sample stage. Topographic STM images are recorded in the constant-current mode at a stabilizing current I between 1 and 2 nA with the bias voltage V applied to the tip. By measuring the differential conductance dI/dV as a function of the sample bias V with lock-in technique [$V_{\mathrm{mod}} = 6\,\mathrm{mV}$ (rms), $f = 786\,\mathrm{Hz}$] dI/dV-maps are obtained. The dI/dV map approximately shows the local density of states (LDOS) of the sample surface at an electron energy E with respect to the Fermi energy E_F [20]. For the image processing we used WSXM [21].

For the step decoration by submonolayer coverages, we follow previous studies of the growth of Fe, Co, Cr, and Ag on Re(0001) [19,22]. At room temperature, Au and Ni grow at submonolayer coverage as compact single-layer islands. The island edges are mostly formed by close-packed atomic rows in three equivalent directions corresponding to the symmetry of the Re(0001) crystal lattice, marked in Fig. 1(c) by black arrows. Low-energy electron diffraction (LEED) measurements of single-monolayer Au and Ni coverages show no extra reflexes [Fig. 1(d)]. Hence, the initial growth of both

*joregel@uni-mainz.de

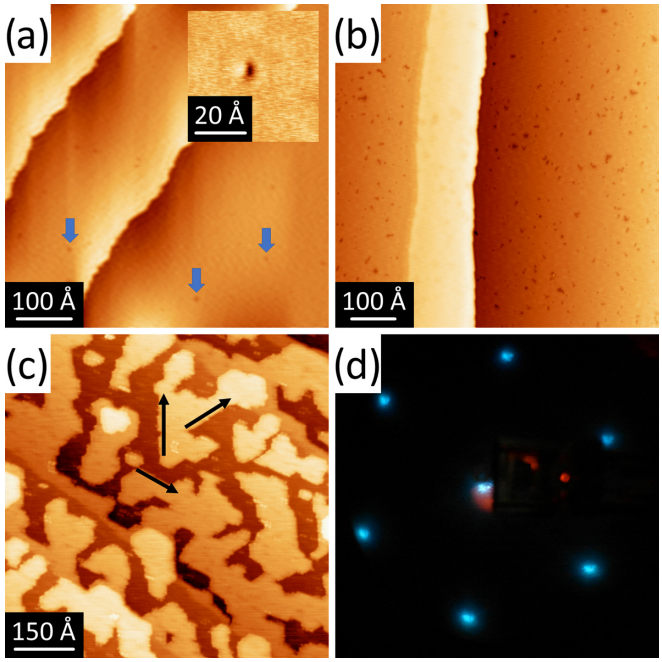

FIG. 1. (a) Constant-current image of the cleaned Re(0001) surface ($V = 100$ mV, $I = 2$ nA); the blue arrows mark point defects appearing as dark spots due to a lower LDOS. The inset shows a magnified image of the defect ($V = -250$ mV, $I = 3$ nA). The elliptical shape with a size of 2×1 Å is likely caused by adsorbed residual gas molecules. (b) The Re surface covered with 0.15 monolayer of Au after annealing ($V = 50$ mV, $I = 2$ nA). The Au forms a bright stripe attached to the step edge. (c) Au islands on Re before annealing ($V = -1$ V, $I = 0.5$ nA). The arrows mark the three crystal axes of preferred island edges. (d) LEED image (electron energy of 40 eV) of the Re/Au surface, showing six low-index reflexes, indicating pseudomorphic growth of the first layer. The red reflexes originate from the camera capturing the LEED image.

metals is pseudomorphic. Starting with the second layer, Au and Ni grow with a different lattice constant, revealing superstructure spots in the LEED images and moiré patterns in the topographic STM images.

III. RESULTS

Figure 1(a) shows a constant-current image of the clean Re(0001) surface at 4.6 K. The Re surface shows large atomically flat regions with terraces of different heights, separated by monoatomic step edges. The topographic troughs directly correspond to a few single-molecule defects appearing as dark spots marked by blue arrows. The defects appear as dark spots due to a lower LDOS, possibly indicating adsorbed CO molecules or oxygen atoms remaining from the cleaning process [19].

A 0.15 monolayer (ML) Au/Re(0001) surface is shown in Fig. 1(b). Here, the step edge runs vertically, and there is a brighter Au stripe attached to the edge. On the Au/Re(0001) surface a larger number of defects appears with respect to pristine Re, likely caused by the increased pressure during the Au evaporation process. A similar topography has been observed for submonolayer coverages of Ni.

To further study the electronic states, we measured spectroscopic dI/dV maps on the pristine Re(0001) surface and on the Re(0001) surface with submonolayer coverages of Au and Ni. Figure 2 shows representative dI/dV maps at various energies and two different surfaces: Re(0001) [Figs. 2(a)–2(e)] and Re/Au [Figs. 2(f)–2(j)]. They were measured in the same region as in Figs. 1(a) and 1(b). The dI/dV maps show quantum interference patterns originating from reflection of electron waves from defects. Step edges, representing a one-dimensional defect, result in a planar wave front, while point defects cause concentric patterns. The images display results for five different energies, as indicated in Fig. 2, to show the energy-dependent wavelengths of the standing wave pattern. The wavelength is directly related to the dispersion relation of the surface bands [15,16]. The quasiparticle interference pattern is caused by the scattering between initial and final states at the same constant-energy contour in momentum space. For binding energies above 0.35 eV and below 0.2 eV, the amplitude of the quasi particle interference (QPI) pattern becomes very weak, preventing the determination of the wavelength. The decreasing amplitude might be caused by an increasing hybridization with bulk states.

The power map of the two-dimensional Fourier transformation [FT; Figs. 2(k)–2(t)] reveals a centered ring-shaped feature that is caused by the quantum interference pattern. The diameter increases with decreasing energy, reflecting the decreasing wavelength in the dI/dV maps. The ring-shaped feature indicates an isotropic effective mass of the corresponding surface state [23]. Two intensity maxima on the ring are caused by the planar wave front originating from the step edges. The fanning-out lines, which are rotated by 90° relative to the step direction in the real-space image, originate from the step edges, too. The dI/dV and power maps for submonolayer coverages of Ni look very similar to those of Au-covered surfaces.

Additional ring-shaped features appearing in some power maps [as marked in Fig. 2(r)] are caused by the stabilization voltage for the tip height in constant-current mode [24]. This artifact arises from spatial modulations in the transmission function due to variations in z at each (x, y) pixel that are dependent on the set-point conditions. Figures 2(g) and 2(h) show a quantum interference pattern on the thin Au stripe. For more accurate data this pattern was investigated on a Re surface covered with 0.95 ML Au. The pattern can be observed in an energy range from 80 to -25 meV and indicates the presence of a surface state on the monolayer Au on Re(0001), too. On the Ni monolayer there is no comparable pattern visible.

For evaluation of the FT power map a radial average over the whole image area was used. The maxima were determined using a Gaussian fit. The resulting dispersion relations, shown in Fig. 3, were obtained by averaging five to ten independent measurements. Within error limits the dispersion relation is identical for pristine Re, Au/Re, and Ni/Re. This is also shown by the effective masses of $m^*_{\mathrm{Re}} = -0.30m_e \pm 0.01m_e$, $m^*_{\mathrm{Re/Au}} = -0.31m_e \pm 0.01m_e$, and $m^*_{\mathrm{Re/Ni}} = -0.30m_e \pm 0.01m_e$ determined at the Γ point via the parabolic fits. The result is also in good agreement with angle-resolved photoemission spectroscopy (ARPES) measurements and density-functional theory calculations [14].

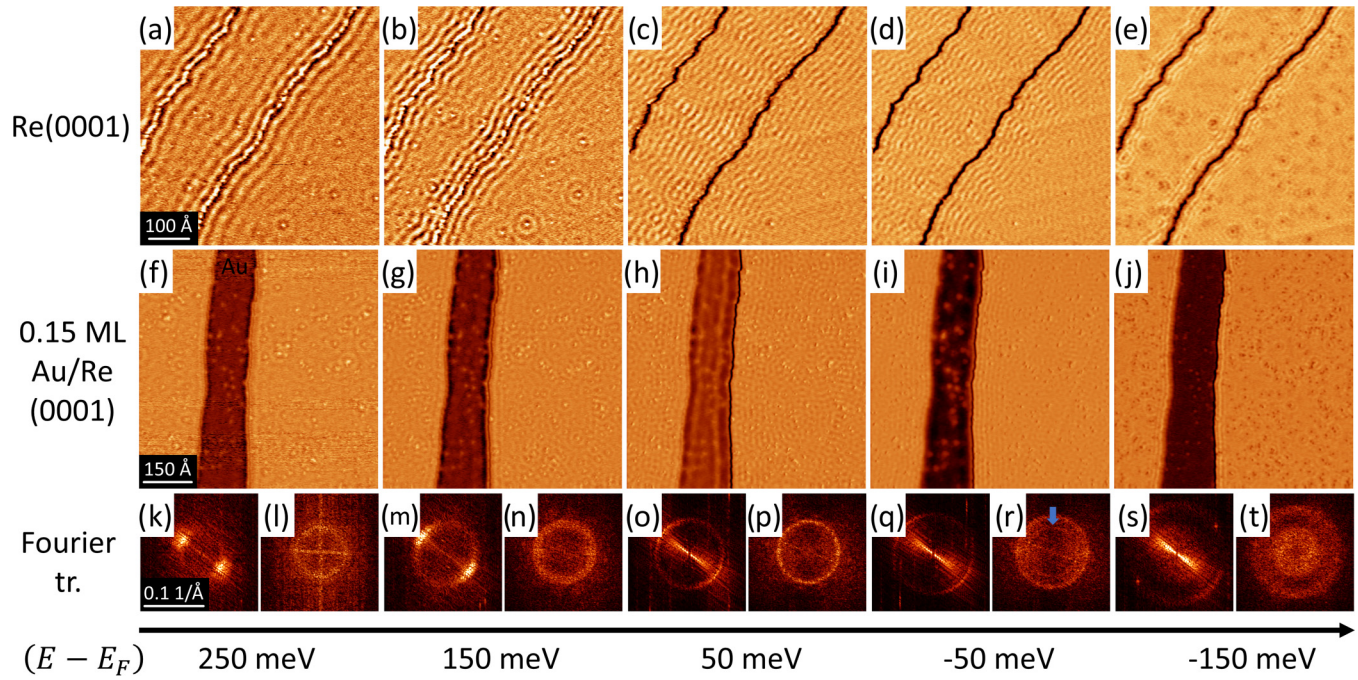

FIG. 2. Quantum interference patterns at different energies (a)–(e) on Re(0001) and (f)–(j) on 0.15 ML Au/Re(0001); dI/dV maps were recorded with tunneling parameters of $I = 2$ nA, $V_{\text{mod}} = 6$ mA, and variable tip-sample voltage. Corresponding topographic images are shown in Fig. 1(a) and 1(b). The evaporated and annealed Au coverage in the second row covers about 15% of the surface. (k)–(t) Power maps from two-dimensional Fourier transformation of the dI/dV maps for clean [(k), (m), (o), (q), and (s)] and Au-covered [(l), (n), (p), (r), and (t)] Re(0001). The double-ring phenomenon, marked, for example, in (r) by a blue arrow, is discussed in the text.

However, because the density-of-states oscillations are generated by a linear combination of the Rashba-split wave vectors, the presence of the Rashba effect could not be verified by FT of STS measurements [7,8].

Quantum interference patterns result from scattering events, where the scattering wave vector combines two states with opposite momenta. For a spin momentum locked Rashba state interband backscattering is forbidden to first order. Intraband scattering from the inner to the outer Rashba band is allowed instead. The scattering vectors of inter- and intraband scattering differ slightly. Small differences between ARPES and STM data may reflect this difference, hinting at interband scattering.

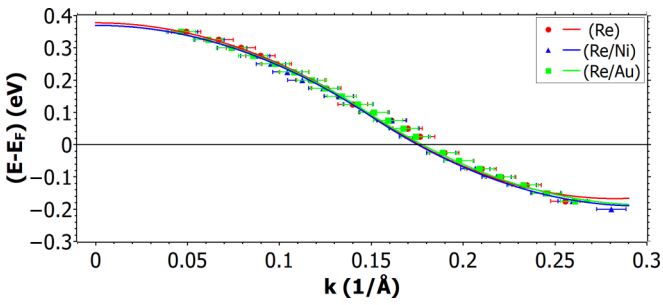

FIG. 3. Energy dispersion relation (energy vs wave number) deduced from Fourier power maps for the three samples, pristine Re(0001), 0.15 ML Au/Re(0001), and 0.15 ML Ni/Re(0001). For the data acquisition five to ten series of measurements were averaged. There are no significant differences between the results for the three samples. The solid line is a plot of two parabolas, which are connected continuously at the inflection point. Because of the continuity condition, the lower parabola has only one free parameter and fits slightly less accurately than the parabola at the Γ point.

For further analysis we discuss the decay of the scattering amplitude with increasing distance from the step edge. Reference [25] reports that a prohibited scattering process leads to a more rapid decay of the standing wave pattern than an allowed scattering process. The attenuation factor has been experimentally and theoretically investigated for various materials, resulting in an exponent of $\beta = -1/2$ for allowed backscattering and $\beta = -3/2$ for forbidden backscattering regarding the following fit function:

$$A = A_0 \sin(bx + c)\left(\frac{x}{x_0}\right)^{\beta} + d. \tag{1}$$

Figure 4 shows the analysis of the pattern attenuation at the step edges on pristine Re as well as on the surfaces with step decorations. Table I summarizes the fitted values for β. The attenuation exponent varies between upper and lower terraces. For the upper terrace $\beta \approx -1/2$ was determined, while for the lower terrace the value is $\beta \approx -3/2$. The comparison of the experimental data (Fig. 4) with the fitted curve and with both model values indicates the significance of this result. Remaining differences of model values and fitted values showed up in other measurements as well [26].

We assume that the differences are explained by the fact that the surface state (SS) on the lower terrace scatters partially into bulk states. This scattering into bulk states is not possible on the upper terrace for geometrical reasons. Therefore, fewer electrons will be backscattered on the lower

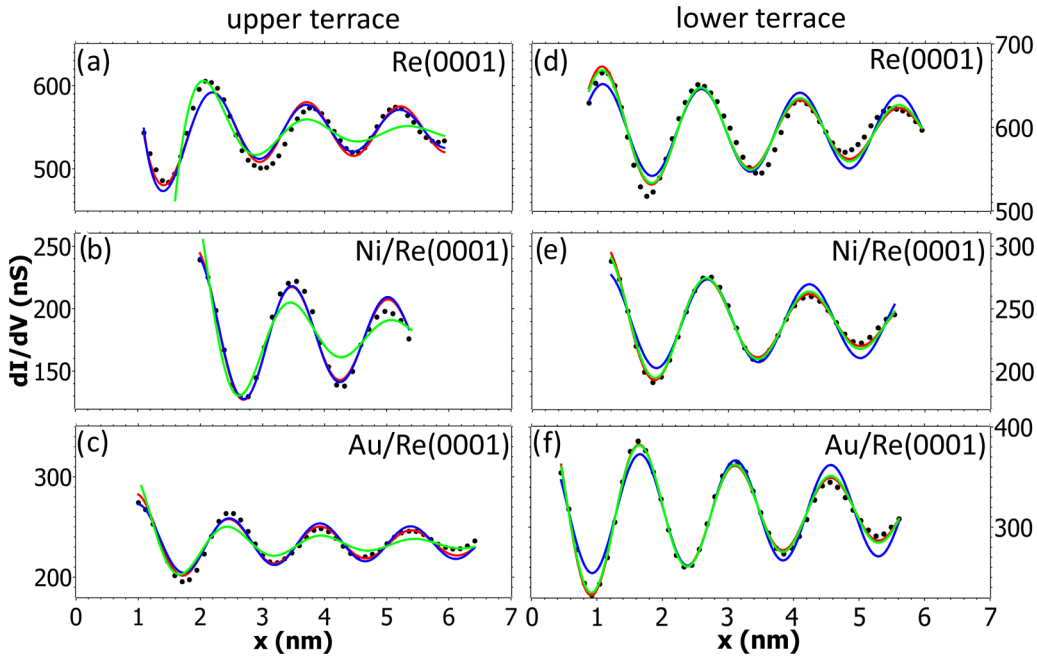

FIG. 4. Examples of the attenuation of quantum interference patterns at a step edge of (a) the pristine Re, (b) the Ni/Re and (c) the Au/Re surfaces, measured with tunneling parameters $V = 100$ mV, $I = 2$ nA, $V_{\mathrm{mod}} = 6$ mV. The solid red line is the fit with Eq. (1) with parameters presented in Table I. The blue (green) line represents Eq. (1) with an exponent of $\beta = -1/2$ ($\beta = -3/2$). A significant difference between upper and lower terraces is noticeable.

terrace, which leads to a faster decay of the QPI pattern. Another reason for the different attenuation behaviors on both sides of the step edge is the so-called smoothing effect [27], which causes the electron density not to follow the sudden change in geometry but to change smoothly from the upper to the lower terrace [28].

The surface state on the upper terrace is thus not suppressed for other reasons, and we take the data for the upper terrace for comparison with the model discussed in Ref. [25]. Thus, the smaller attenuation exponent of $\beta = -1/2$ determined for the unperturbed surface state on the upper terrace indicates an allowed interband scattering process.

The analysis of the phase angle of the QPI pattern reveals a direct connection to the energy barrier: a phase of 0° implies a fixed end and a barrier wall with infinite height. A phase of 180° would correspond to a loose end with a negative energy barrier. Figure 5 illustrates the data evaluation process for the extraction of the phase with an example for pristine Re [Figs. 5(a)–5(d)] and one for Re/Au [Figs. 5(e)–5(h)]. The topographic images [Figs. 5(a) and 5(e)] are used to determine the center of the step edge in half of the height decrease or increase in the height profiles shown in Figs. 5(b) and 5(f). The simultaneously recorded dI/dV maps of the identical regions reveal the QPI pattern [Figs. 5(c) and 5(g)]. The corresponding profile of the dI/dV modulation [Figs. 5(d) and 5(h)] is separately fitted by Eq. (1) for the upper terrace with $\beta = -1/2$ and for the lower terrace with $\beta = -3/2$.

In the example, the reverse phase relationship between Re and Re/Au can clearly be seen. In Fig. 5(d) both fits subtend the step edge at the maximum of about 90°, with the intersection points varying slightly. The Re/Au sample behaves contrarily at the same energy: the extrapolated wave of the upper terrace crosses the step edge at the minimum of about 270°, as can also be seen in Fig. 6. The intersection of the surface wave on the lower terrace is at about 40°. The behavior changes when the sign of the tip-sample voltage changes, which leads to the characteristic phase jump.

In both wave profiles the red fit is more accurate than the green one. This is due to the fact that the first crest of the wave on the lower terrace, marked by a red arrow, does not match the surface state in amplitude and wavelength but is manipulated by the potential of the step edge. Therefore, the surface state was fitted from only the second peak onwards and extrapolated over the distance to the step edge. Even small imperfections have considerable effects on the wave profile. For example, the defect marked with a blue arrow in Fig. 5(c) changes the amplitude and wavelength of the last peak marked with a black arrow in Fig. 5(d). On the Re/Au sample, these effects were amplified by the higher

TABLE I. Calculated attenuation parameters for the measured wave patterns. The first row in each set is related to the data in Fig. 4, and the second row shows averages over all energies from −125 to 150 meV with the standard deviation of the mean value, representing a statistical error.

	Re	Ni/Re	Au/Re
	Upper terrace		
Fig. 4	−0.37	−0.78	−0.59
Average	−0.52 ± 0.02	−0.66 ± 0.01	−0.70 ± 0.01
	Lower terrace		
Fig. 4	−1.81	−1.65	−1.79
Average	−1.37 ± 0.16	−1.66 ± 0.06	−1.94 ± 0.14

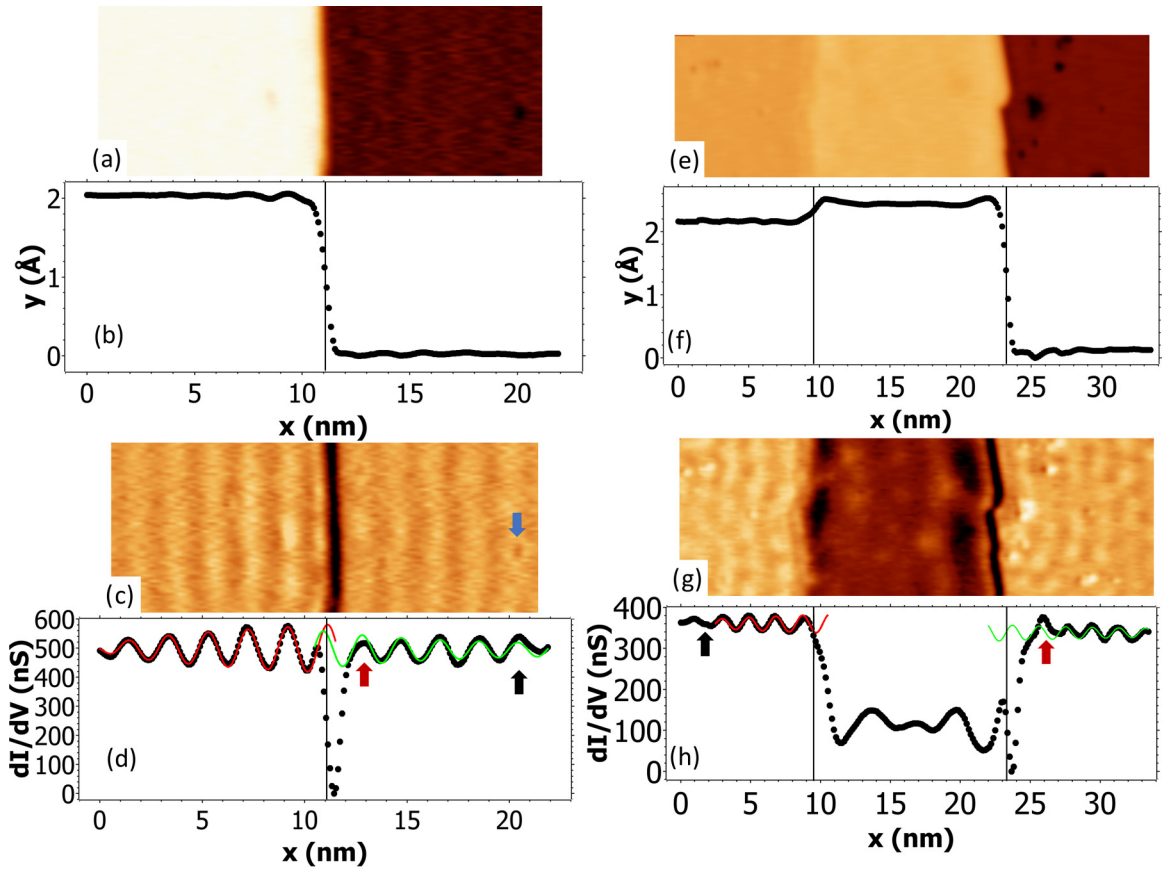

FIG. 5. Two examples for the determination of phase angles at an energy of $V = 75$ mV with a tunneling current of $I = 2$ nA. (a) and (e) Topographic images of a step edge running vertically through the image on (a) Re and (e) 0.15 ML Re/Au. (b) and (f) Height profiles along the horizontal axis. (c) and (g) Differential conductivity maps from the identical region shown in (a) and (e). (d) and (h) Profiles of the dI/dV values along the horizontal axis. By fitting and extrapolating the profile (red and green solid lines) to the center of the step edge (vertical black lines), the phase angle was determined. The red fits on the upper terraces were fitted by using Eq. (1) with $\beta = -1/2$; the green fits on the lower terraces were fitted with $\beta = -3/2$.

defect density (black arrow). Due to the fringy step decoration it is often not possible to obtain parallel wave crests over larger areas, which leads to the fluctuating amplitude and a particularly distorted first-wave crest as in Fig. 5(h). For this reason, narrower profiles were usually used to analyze the phase angles.

Figure 6 summarizes the fit values for the phase for all samples and higher and lower terraces, respectively. The striking observation is a phase shift of about 180° at E_F, which is reflected in all measurements, independent of the step decoration. The error bars shown in the plots represent statistical errors resulting from averaging four measurements each. We are aware of additional systematic errors of the fit procedure, for example, the precise position of the step edge. The variation of the step edge position would result in a common shift of all phase angle values yet not eliminate the phase jump at E_F.

In addition to the phase shift, linear tendencies can be seen. With increasing energy one observes a linear increase or decrease of the phase, which might be attributed to a change in the effective barrier height with energy. Generally, the lower range of phase angles is between 50° and 150°, and the upper range is between 250° and 350°. An average phase jump of less than 180° indicates a medium barrier height. The occurrence of the phase shift can be explained with the following model. With the STM, unoccupied sample states are investigated with negative voltages, and occupied sample states are investigated with positive voltages. Unoccupied states are known in semiconductor physics as holes with positive charge; occupied states are electrons with negative charge. A potential barrier behaving like a wall for electrons will become a valley for holes because of the opposite charge, resulting in a phase jump of approximately 180°.

While there is little difference between the upper and lower terraces for Re and Re/Ni, there is a significant difference for Re/Au: the phase shift is reversed on the upper terrace side of the step with respect to the other cases. This behavior is likely caused by the previously mentioned surface state on gold. On the upper terrace the Au surface state and the SS on Re(0001) are coupled. Such a coupling is enabled by the fact that the topmost Re layer on the upper terrace is continued by the topmost Au layer at the same height. The line boundary between the topmost Re and Au layers is the one-dimensional analog to a two-dimensional metal-metal interface. The coupling of surface states is not possible on the lower terrace because the Re(0001) surface layer is not continued at the same height; hence, the behavior does not differ from the other step decorations.

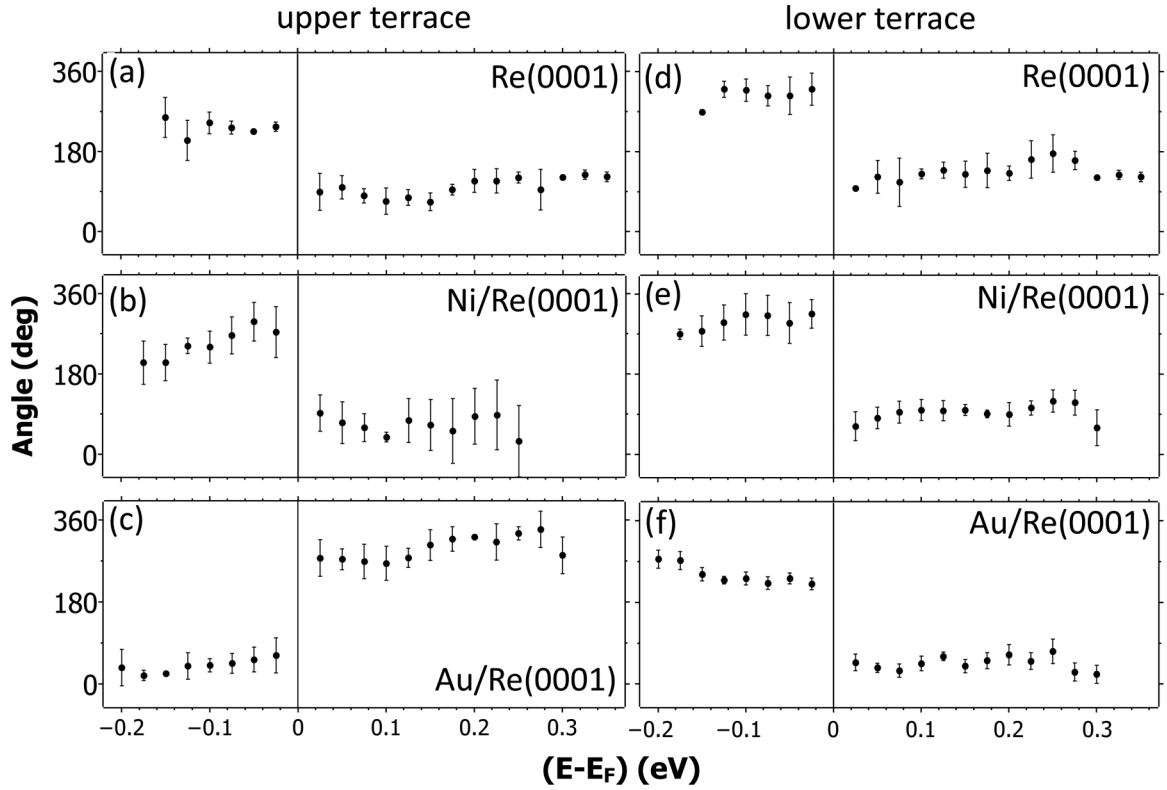

FIG. 6. The phase angles of the QPI at the step edge determined on the (a)–(c) upper and (d)–(f) lower terraces. The phase is determined with respect to the center of the step edge (Fig. 5). Shown on (a) and (d) pristine Re(0001), (b) and (e) Re(0001) with 0.15 ML Ni evaporated, and (c) and (f) Re(0001) with 0.15 ML Au evaporated. The phase shift at E_F where Au stands out with a reverse behavior is remarkable.

IV. SUMMARY

In conclusion, the energy dependence of the phase and wavelength of quantum interference patterns on Re(0001) was investigated by scanning tunneling spectroscopy. The energy dispersion relation of the corresponding surface state as deduced from Fourier transformation is independent of the momentum direction. The analysis of the attenuation of the quantum interference pattern with increasing distance from a declining step edge indicates interband scattering between the two branches of the Rashba-split surface band. The interband scattering is also confirmed by a comparison of the dispersion relation with results from angular-resolved photoemission [14].

The attenuation with distance is considerably larger at a rising step edge, which is tentatively explained by hybridization of surface and bulk states combined with an increased absorption probability. To test if spin-orbit or magnetic exchange scattering might change the interband to intraband scattering, which is forbidden without spin flip, step edges were decorated with submonolayer Au and Ni stripes grown by step-flow growth starting at the Re(0001) step edges. The energy dispersion relation and the attenuation behavior do not change for these step decorations. This result indicates that spin-flip processes do not significantly contribute to the formation of quantum interference patterns.

The phase of the step-induced QPI pattern shows a π shift for a sign change of the tunneling current. This shift points to a change of the scattering energy barrier from a potential dike for electrons to a potential trench for holes. A striking change to the opposite behavior is observed at the higher surface terrace if the top layer changes from Re to Au. In this case, representing the one-dimensional analog to a metal-metal layer interface, the Re surface state continues on the 1 ML Au/Re(0001) surface, showing a similar QPI pattern. The continuation of the surface state across the one-dimensional interface reverses the scattering barrier behavior.

ACKNOWLEDGMENT

Funding by the Deutsche Forschungsgemeinschaft (DFG, German Research Foundation), Grant No. TRR 173-268565370 (project A09), is gratefully acknowledged.

[1] E. I. Rashba, Sov. Phys. **2**, 1109 (1960).

[2] P. Roushan, J. Seo, C. V. Parker, Y. S. Hor, D. Hsieh, D. Qian, A. Richardella, M. Z. Hasan, R. J. Cava, and A. Yazdani, Nature (London) **460**, 1106 (2009).

[3] Z. Alpichshev, J. G. Analytis, J.-H. Chu, I. R. Fisher, Y. L. Chen, Z. X. Shen, A. Fang, and A. Kapitulnik, Phys. Rev. Lett. **104**, 016401 (2010).

[4] L. El-Kareh, P. Sessi, T. Bathon, and M. Bode, Phys. Rev. Lett. **110**, 176803 (2013).

[5] L. El-Kareh, G. Bihlmayer, A. Buchter, H. Bentmann, S. Blügel, F. Reinert, and M. Bode, New J. Phys. **16**, 045017 (2014).
[6] M. Steinbrecher, H. Harutyunyan, C. R. Ast, and D. Wegner, Phys. Rev. B **87**, 245436 (2013).
[7] L. Petersen and P. Hedegård, Surf. Sci. **459**, 49 (2000).
[8] J. I. Pascual, G. Bihlmayer, Y. M. Koroteev, H.-P. Rust, G. Ceballos, M. Hansmann, K. Horn, E. V. Chulkov, S. Blügel, P. M. Echenique, and P. Hofmann, Phys. Rev. Lett. **93**, 196802 (2004).
[9] H. Zhang, F. Freimuth, G. Bihlmayer, M. Ležaić, S. Blügel, and Y. Mokrousov, Phys. Rev. B **87**, 205132 (2013).
[10] A. Stróżecka, A. Eiguren, and J. I. Pascual, Phys. Rev. Lett. **107**, 186805 (2011).
[11] D. Hsieh, Y. X. L. Wray, D. Qian, A. Pal, J. H. Dil, J. Osterwalder, F. Meier, G. Bihlmayer, C. L. Kane, Y. S. Hor, R. J. Cava, and M. Z. Hasan, Science **323**, 919 (2009).
[12] X. Zhou, C. Fang, W.-F. Tsai, and J. P. Hu, Phys. Rev. B **80**, 245317 (2009).
[13] A. Urru and A. D. Corso, Surf. Sci. **686**, 22 (2019).
[14] H. J. Elmers, J. Regel, T. Mashoff, J. Braun, S. Babenkov, S. Chernov, O. Fedchenko, K. Medjanik, D. Vasilyev, J. Minar, H. Ebert, and G. Schönhense, Phys. Rev. Research **2**, 013296 (2020).
[15] M. F. Crommie, C. P. Lutz, and D. M. Eigler, Nature (London) **363**, 524 (1993).
[16] Y. Hasegawa and P. Avouris, Phys. Rev. Lett. **71**, 1071 (1993).
[17] J. Li, W. D. Schneider, and R. Berndt, Phys. Rev. B **56**, 7656 (1997).
[18] S. LaShell, B. A. McDougall, and E. Jensen, Phys. Rev. Lett. **77**, 3419 (1996).
[19] S. Ouazi, T. Pohlmann, A. Kubetzka, K. von Bergmann, and R. Wiesendanger, Surf. Sci. **630**, 280 (2014).
[20] J. Tersoff and D. R. Hamann, Phys. Rev. Lett. **50**, 1998 (1983).
[21] I. Horcas and R. Fernández, Rev. Sci. Instrum. **78**, 013705 (2007).
[22] M. Parschau, D. Schlatterbeck, and K. Christmann, Surf. Sci. **376**, 133 (1997).
[23] L. Petersen, P. T. Sprunger, Ph. Hofmann, E. Lægsgaard, B. G. Briner, M. Doering, H.-P. Rust, A. M. Bradshaw, F. Besenbacherc, and E. W. Plummer, Phys. Rev. B **57**, R6858 (1998).
[24] A. J. Macdonald, Y.-S. Tremblay-Johnston, S. Grothe, S. Chi, P. Dosanjh, S. Johnston, and S. A. Burke, Nanotechnology **27**, 414004 (2016).
[25] J. Wang, W. Li, P. Cheng, C. Song, T. Zhang, P. Deng, X. Chen, X. Ma, K. He, J.-F. Jia, Q.-K. Xue, and B.-F. Zhu, Phys. Rev. B **84**, 235447 (2011).
[26] Ph. Avouris, I.-W. Lyo, and P. Molinàs-Mata, Chem. Phys. **240**, 423 (1995).
[27] R. Smoluchowski, Phys. Rev. **60**, 661 (1941).
[28] P. Avouris and I.-W. Lyo, Science **264**, 942 (1994).